PHYSICAL REVIEW D **107,** 075040 (2023)

Resonant top pair searches at the LHC: A window to the electroweak phase transition

Dorival Gonçalves,[1,*] Ajay Kaladharan,[1,†] and Yongcheng Wu[2,1,‡]
[1]*Department of Physics, Oklahoma State University, Stillwater, Oklahoma 74078, USA*
[2]*Department of Physics and Institute of Theoretical Physics, Nanjing Normal University, Nanjing, 210023, China*

(Received 28 June 2022; accepted 15 April 2023; published 28 April 2023)

The dynamics of electroweak phase transition could have profound consequences for particle physics and cosmology. We study the prospects for the HL-LHC to probe the strong first-order electroweak phase transition (SFOEWPT) regime in the type-I 2HDM. We focus on the Higgstrahlung channel $pp \to ZH/A$ with a resonant top-quark pair final state $H/A \to t\bar{t}$. We find that the top-quark pair final state renders the largest sensitivity to the SFOEWPT regime, in comparison to the other Higgstrahlung searches already performed by ATLAS and CMS, that focus on the $H/A \to bb$ and $H \to WW$ final states. We also derive the complementarity of the Higgstrahlung searches with other relevant classes of searches at the HL-LHC and compare them with the gravitational wave sensitivity at LISA.

DOI: 10.1103/PhysRevD.107.075040

I. INTRODUCTION

The electroweak symmetry appears exact in the early Universe at high temperatures. However, at temperatures around 100 GeV, the Higgs field develops a vacuum expectation value, spontaneously breaking this symmetry. At this time, the Universe goes through a transition from a symmetric to a broken phase. While the Standard Model (SM) predicts a continuous transition [1], new physics can generate a first-order phase transition. As yet, it is unknown how the electroweak phase transition (EWPT) occurred—whether it was violent or calm; first-order phase transition or smooth crossover.

First-order phase transition is a violent phenomenon that can display relevant consequences for the evolution of the Universe. In particular, this transition could provide the required out-of-equilibrium conditions to generate the baryon asymmetry of the Universe via electroweak baryogenesis [2–6]. If the first-order phase transition was strong enough, it could have generated relic gravitational waves (GW) that might be probed in future GW detectors, such as in the space-based LISA mission [7,8]. This transfiguration in the EWPT profile usually requires novel degrees of freedom close to the electroweak scale, displaying sizable interactions with the Higgs boson [9,10]. Thus, precision measurements for the Higgs sector and the search for new heavy scalars at colliders are also important avenues for probing models which trigger first-order electroweak phase transition. The Higgs pair production $pp \to hh$ plays a central role in these studies, as it provides a direct probe to the Higgs potential through resonant and nonresonant searches [11–15]. Thus, this subject provides an exciting research arena on the interface between particle physics and cosmology.

The strength of the phase transition is correlated with the potential upliftment of the true vacuum compared to the symmetric one at zero temperature [16–18]. This gauge-invariant property sheds light on the phase transition pattern analytically. In particular, it is possible to derive that the large order parameter, $\xi_c \equiv v_c/T_c \gtrsim 1$, favors light scalar masses [10]. This grants extra motivation for resonant searches at the Large Hadron Collider (LHC). Besides scalar masses under the TeV scale, the analytical structure of the beyond the SM effects on the vacuum upliftment, leading to strong first-order electroweak phase transition (SFOEWPT), $\xi_c \gtrsim 1$, results in a distinct hierarchy of masses among the new scalar states.

In the two Higgs doublet model (2HDM) [16,19–33], the parameter space $m_H < m_{H^\pm} \approx m_A$, with large mass difference, yields a favorable regime to achieve SFOEWPT [10,34]. Due to the preference for large mass hierarchy among the scalar modes, it is likely that at least one of the scalar states is above the top-quark pair threshold. As recently shown, the gluon fusion production channel $gg \to A/H \to t\bar{t}$ plays a leading role in these phenomenological

---

[*]dorival@okstate.edu
[†]kaladharan.ajay@okstate.edu
[‡]ycwu@njnu.edu.cn

studies, granted by its large event rate [10]. Another relevant channel is the resonant Higgstrahlung production 34] $A \to ZH$], which is enhanced in the preferred scalar mass regime for SFOEWPT, $m_H < m_{H^\pm} \approx m_A$. However, the current experimental analyses explore the $A \to ZH$ searches only through the decays $H \to b\bar{b}$ and $H \to WW$ with $Z \to \ell\ell$ [35]. The flipped channel $H \to ZA$ is also analyzed with $A \to b\bar{b}$ and $Z \to \ell\ell$ [36]. For $A \to ZH$ or $H \to ZA$ channels, the corresponding heavy scalar decay to top-quark pair $H/A \to t\bar{t}$ can also be an important signature for the SFOEWPT parameter space. Compared to the already explored scalar decays to $b\bar{b}$ and W^+W^-, the $t\bar{t}$ final state covers a different mass spectrum, which can significantly improve the sensitivity of $A \to ZH$ and $H \to ZA$ channels. In the present work, we scrutinize the sensitivity of the scalar decays to top-quark pair for probing SFOEWPT in the 2HDM. Special attention will be devoted to the Higgstrahlung mode $pp \to ZH/A$ at the high luminosity LHC (HL-LHC).

This paper is organized as follows. In Sec. II, we introduce the two Higgs doublet model. In Sec. III, we discuss the leading contributions for the 2HDM signature $pp \to ZH/A$ with top-quark pair final state $H/A \to t\bar{t}$. The corresponding HL-LHC sensitivity is derived in Sec. IV. In Sec. V, we study the complementarity between collider and gravitational wave experiments to probe the electroweak phase transition profile in the 2HDM. In particular, we scrutinize the relevance of the Higgstrahlung channel with top pair final states $H/A \to t\bar{t}$ with respect to other relevant classes of searches at the HL-LHC. We also contrast the collider with the gravitational wave sensitivity. We summarize in Sec. VI. Further details on the complementary channel $gg \to H/A \to t\bar{t}$ are presented in the Appendix.

II. TWO HIGGS DOUBLET MODEL

In this work, we consider the CP-conserving 2HDM with a softly broken $\mathbb{Z}_2$ symmetry, where the scalar potential can be written as [37]

$$\begin{aligned}V(\Phi_1,\Phi_2) = {}& m_{11}^2\Phi_1^\dagger\Phi_1 + m_{22}^2\Phi_2^\dagger\Phi_2 - m_{12}^2(\Phi_1^\dagger\Phi_2 + \text{H.c.})\\ &+ \frac{\lambda_1}{2}(\Phi_1^\dagger\Phi_1)^2 + \frac{\lambda_2}{2}(\Phi_2^\dagger\Phi_2)^2\\ &+ \lambda_3(\Phi_1^\dagger\Phi_1)(\Phi_2^\dagger\Phi_2) + \lambda_4(\Phi_1^\dagger\Phi_2)(\Phi_2^\dagger\Phi_1)\\ &+ \frac{\lambda_5}{2}((\Phi_1^\dagger\Phi_2)^2 + \text{H.c.}). \qquad (1)\end{aligned}$$

Expanding around the VEVs, the two $SU(2)_L$ doublets can be expressed by

$$\Phi_1 = \begin{pmatrix} \phi_1^+ \\ \frac{v_1+\phi_1^0+i\eta_1}{\sqrt{2}} \end{pmatrix}, \qquad \Phi_2 = \begin{pmatrix} \phi_2^+ \\ \frac{v_2+\phi_2^0+i\eta_2}{\sqrt{2}} \end{pmatrix}, \qquad (2)$$

where the vacuum expectation values v_i are connected to the SM VEV by $v_1^2 + v_2^2 = v^2 \approx (246\ \text{GeV})^2$. After electroweak symmetry breaking, the model provides five physical mass eigenstates from the scalar sector: two CP-even neutral scalars h and H, where h is identified as the SM Higgs boson, a CP-odd neutral scalar A, and a pair of charged scalars $H^\pm$. The mass and gauge eigenstates are related by the rotation angle β for the charged and CP-odd sectors, $\tan\beta \equiv v_2/v_1$, and by the angle α for the CP-even sector

$$\begin{pmatrix} G^\pm \\ H^\pm \end{pmatrix} = \mathcal{R}(\beta)\begin{pmatrix} \phi_1^\pm \\ \phi_2^\pm \end{pmatrix}, \qquad \begin{pmatrix} G^0 \\ A \end{pmatrix} = \mathcal{R}(\beta)\begin{pmatrix} \eta_1 \\ \eta_2 \end{pmatrix},$$
$$\begin{pmatrix} H \\ h \end{pmatrix} = \mathcal{R}(\alpha)\begin{pmatrix} \phi_1^0 \\ \phi_2^0 \end{pmatrix}. \qquad (3)$$

The rotation matrix is given by

$$\mathcal{R}(x) = \begin{pmatrix} c_x & s_x \\ -s_x & c_x \end{pmatrix}, \qquad (4)$$

where $s_x \equiv \sin x$ and $c_x \equiv \cos x$. The charged and neutral massless Goldstone bosons are denoted by $G^\pm$ and G^0, respectively.

The physical parameters of 2HDM can be chosen as

$$\tan\beta, \quad \cos(\beta-\alpha), \quad m_{12}^2, \quad v, \quad m_h(=125\ \text{GeV}),$$
$$m_H, \quad m_A, \quad m_{H^\pm}. \qquad (5)$$

The parameters $t_\beta \equiv \tan\beta$ and $c_{\beta-\alpha} \equiv \cos(\beta-\alpha)$ control the coupling strength of the scalar particles to fermions and gauge bosons, displaying critical phenomenological relevance. Whereas the Higgs-gauge couplings scale as $g_{hVV} \propto s_{\beta-\alpha}$ and $g_{HVV} \propto c_{\beta-\alpha}$, the fermion interactions hinge on both t_β and $c_{\beta-\alpha}$. The fermionic couplings depend on the $\mathbb{Z}_2$ charge assignment in the Yukawa sector. In this study, we focus on the type-I scenario where all fermions couple solely to Φ_2. When confronted with current experimental constraints, the alignment limit $c_{\beta-\alpha} \to 0$ is preferred [38,39]. Furthermore, electroweak precision measurements also put strong constraints on the 2HDM parameter space, which pushes either $\Delta m_H \equiv m_H - m_{H^\pm}$ or $\Delta m_A \equiv m_A - m_{H^\pm}$ close to zero.

III. TOP PAIR RESONANT SEARCHES VIA $pp \to ZH/A$

In this section, we will discuss the dominant contributions for the 2HDM signature $pp \to ZH/A$ with top-quark pair final state $H/A \to t\bar{t}$. The Higgstrahlung channel, $pp \to ZH/A$, has three dominant contributions at the LHC [40]. First, it contains the loop-induced gluon fusion production $gg \to ZH/A$. This mode encapsulates both resonant $gg \to A/H \to ZH/A$ and nonresonant contributions,

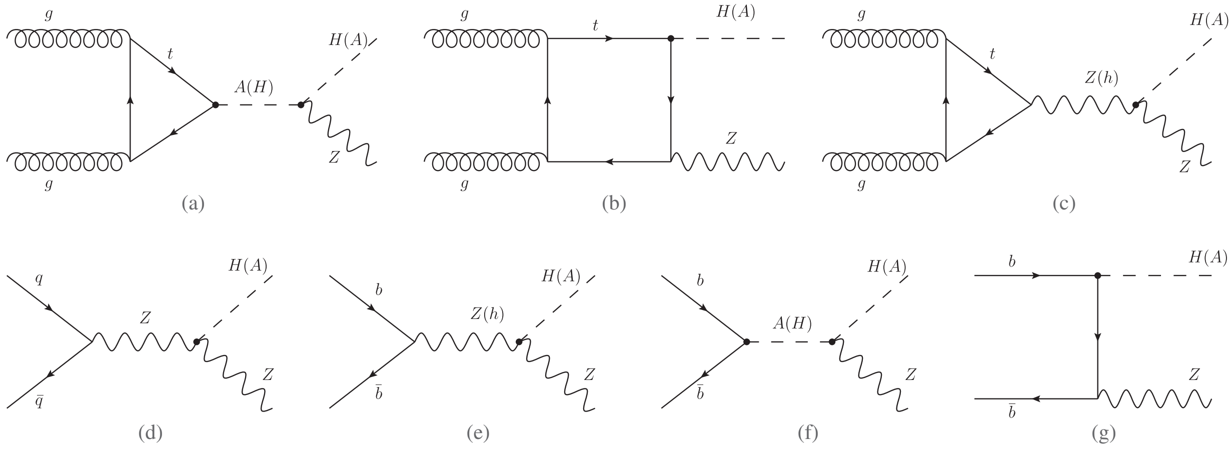

FIG. 1. Representative set of Feynman diagrams for Higgstrahlung production $pp \to ZH/A$ at the LHC: (a–c) loop induced gluon fusion production $gg \to ZH/A$; (d) Drell-Yan like contribution $q\bar{q} \to ZH$; and (e–g) bottom quark initiated production $b\bar{b} \to ZH/A$. We highlight the couplings that differ between the SM and 2HDM.

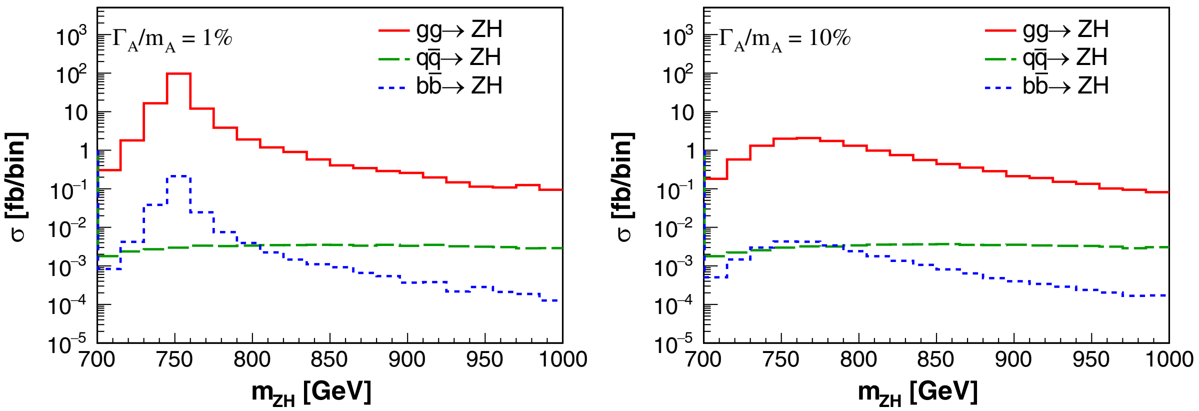

FIG. 2. Invariant mass distribution m_{ZH} for the Higgstrahlung signal $pp \to ZH$ at the parton level with different choice of scalar widths: $\Gamma_A/m_A = 1\%$ (left panel) and $\Gamma_A/m_A = 10\%$ (right panel). We decompose the signal in its leading contributions: (i) loop-induced gluon fusion production $gg \to ZH$ (red); (ii) b-quark initiated production $b\bar{b} \to ZH$ (blue); and (iii) Drell-Yan like contribution $q\bar{q} \to Z^* \to ZH$ (green). For illustration, we consider the type-I 2HDM with maximally allowed mixing angles, giving the current LHC data: $c_{\beta-\alpha} \approx 0.3$. In addition, we assume $m_H = 600$ GeV, $m_A = 750$ GeV, and $t_\beta = 1$.

see Fig. 1(a–c).[1] Another relevant mode stems from the tree-level Drell-Yan-like production, $q\bar{q} \to Z^* \to ZH$, Fig. 1(d). Notably, this production channel does not result in a correspondent ZA final state. This mode is absent at this order of perturbation expansion, as the ZZA coupling is forbidden at tree-level. Finally, there are also important b-quark initiated contributions, $b\bar{b} \to ZH/A$, that can be augmented in the enhanced bottom Yukawa coupling regime, Fig. 1(e–g).

In Fig. 2, we illustrate these three leading contributions to the Higgstrahlung signal $pp \to ZH$. The gluon fusion and bottom quark-initiated channels generally result in significant rates, typically enhanced by intermediate resonant Higgs production $H/A \to ZA/H$. Between these two terms, there are three leading effects that guarantee the dominance of the gluon fusion channel: (i) the gluon fusion channel is driven by the large parton distribution function of initial state gluons; (ii) it has larger initial state color factor; and (iii) the triangle and box diagrams are enhanced by the sizable top Yukawa coupling, shown respectively in Fig. 1(a) and Fig. 1(b). The last term, the Drell-Yan-like mode, generally produces subleading corrections. Its cross section is hampered by the absence of a resonant scalar mode $A \to ZH$ and the dependence with the mixing angle $\sigma_{\mathrm{DY}}^{ZH} \propto c_{\beta-\alpha}^2$. The suppressed rate becomes apparent even when adopting maximally allowed mixing angles. We depict this scenario in Fig. 2, considering the type-I 2HDM with $c_{\beta-\alpha} \approx 0.3$. Remarkably, the type-II scenario

---

[1] Note that we grouped two diagrams with two different types of the propagators in Fig. 1(c), as they share the same scaling behavior as we will discuss in the following. Similar for Fig. 1(e).

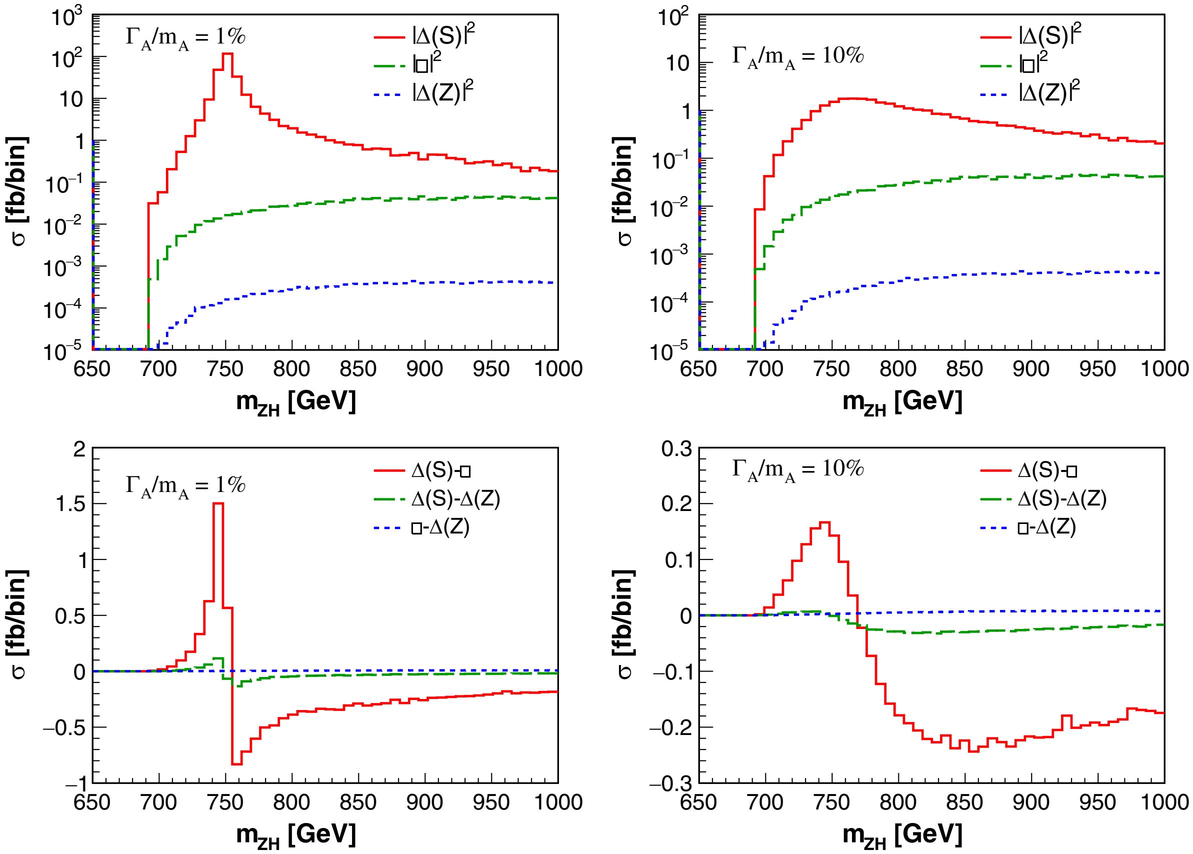

FIG. 3. The distributions of m_{ZH} for $gg \to ZH$, with $m_A = 750$ GeV, $m_H = 600$ GeV, $c_{\beta-\alpha} = 0.1$, and $t_\beta = 1$ in the type-I 2HDM. The width of A is chosen to be 1% (10%) of the mass in left (right) panels. In the upper panels, the red, green, and blue lines correspond to contributions from the individual set of diagrams presented by Fig. 1(a), Fig. 1(b), and Fig. 1(c), respectively. In the lower panels, red, green and blue lines represent the contributions from the interference between different set of diagrams as indicated by the legend.

leads to further depleted Drell-Yan production, as the experimental constraints tend to confine the model parameters further toward the alignment limit, $c_{\beta-\alpha} \to 0$.

Although resonant production $gg \to A/H \to ZH/A$ typically results in high rates, the other gluon fusion contributions present relevant effects that need to be included for a robust simulation. In particular, the triangle and box diagrams depicted in Fig. 1(a) and Fig. 1(b) display sizable interference effects, which significantly depend on the scalar and pseudo-scalar particle widths. To illustrate it, we present in Fig. 3 the parton level distributions m_{ZH} obtained for a benchmark point with $m_H = 600$ GeV, $m_A = 750$ GeV, $c_{\beta-\alpha} = 0.1$, and $t_\beta = 1$. The widths for A and H are chosen to be $\Gamma_{H,A}/m_{H,A} = 1\%$ (left panel) and 10% (right panel). We present the separate components of the signal process in the top panel, including triangle diagrams mediated by a A-mediated resonance only (red), box diagrams only (green), Z-mediated diagrams only (blue). The respective interferences contributions are shown in the bottom panels of the same figure. The resonant production $gg \to A \to ZH$ results in leading effects, followed by its interference with the box contributions. In general, there is also interference between the signal with the $t\bar{t}Z$ background. However, as checked numerically, such interference generates only subleading rates for the allowed 2HDM parameter space.

IV. ANALYSIS

In this section, we derive the sensitivity to the Higgstrahlung signals $pp \to Z(\ell\ell)H(t\bar{t})$ and $pp \to Z(\ell\ell)A(t\bar{t})$ at the $\sqrt{s} = 14$ TeV HL-LHC. The analysis focus on the semileptonic top pair final state. The leading background for this process arises from $t\bar{t}Z$ production. In our study, the Monte Carlo event generation is performed with MadGraph5aMC@NLO_v3.1.1 [41], where the 2HDM model file is prepared with FEYNRULES [42] and NLOCT [43].[2] This model allows the computation of tree-level and one-loop amplitudes. The hadronization and underlying event effects are simulated with PYTHIA_v8.306 [44]. Detector effects are accounted for by DELPHES_v3.5.0 [45] package.

---

[2] One can find the UFO model files for 2HDM at https://github.com/ycwu1030/2HDM_FR.

TABLE I. Couplings involved in the diagrams of Fig. 1, where $\kappa_f^A = 1/t_\beta$, $\kappa_f^H = s_\alpha/s_\beta$, $\kappa_V = c_{\beta-\alpha}$, and $\kappa_V' = s_{\beta-\alpha}$.

Contribution	Fig. 1(a)	Fig. 1(b)	Fig. 1(c)	Fig. 1(d)	Fig. 1(e)	Fig. 1(f)	Fig. 1(g)
κ's for ZH	$\kappa_f^A \kappa_V' \kappa_f^H$	$\kappa_f^H \kappa_f^H$	$\kappa_V \kappa_f^H$	$\kappa_V \kappa_f^H$	$\kappa_V \kappa_f^H$	$\kappa_f^A \kappa_V' \kappa_f^H$	$\kappa_f^H \kappa_f^H$
κ's for ZA	$\kappa_f^H \kappa_V' \kappa_f^A$	$\kappa_f^A \kappa_f^A$	$\kappa_V \kappa_f^A$	$\cdots$	$\kappa_V \kappa_f^A$	$\kappa_f^H \kappa_V' \kappa_f^A$	$\kappa_f^A \kappa_f^A$

The simulation is performed on a grid spanned in four parameters $(m_A, m_H, \Gamma_A, \Gamma_H)$, setting $t_\beta = 1$ and $c_{\beta-\alpha} = 0.1$. The proper values of t_β and $c_{\beta-\alpha}$ will be adjusted later, satisfying the scan on the parameters of Eq. (5). For m_A and m_H, we scan the light scalar mode within [400, 750] GeV with 50 GeV step size, while the more massive one will be at least 100 GeV heavier to allow for the decay $A/H \to ZH/A$ and within [500, 850] GeV with 50 GeV step size. For the widths, we follow the same grid adopted by CMS in Ref. [46] for their $gg \to H/A \to t\bar{t}$ analysis, such that $\Gamma_{A/H}/m_{A/H} = 0.5\%, 1.0\%, 2.5\%, 5.0\%, 10.0\%, 25.0\%$. For any other values of masses and widths obtained in our parameter scan, interpolation will be used to extract the corresponding results. To easily cover all other possible choices of parameters, the generation of resonant and interference terms for the signal is performed separately for contributions with distinct dependence on t_β and $c_{\beta-\alpha}$. Hence, for any other case, we can scale the result according to the corresponding dependence on t_β and $c_{\beta-\alpha}$. The dependence of each diagram on t_β and $c_{\beta-\alpha}$ is listed in Table I.[3] The procedure described in this paragraph will allow for a more effective scan of the model parameters. In particular, this will be relevant for the broad parameter space scan of the type-I 2HDM performed in Sec. V.

In our event analysis, we require three isolated leptons with $p_{T\ell} > 20$ GeV and $|\eta_\ell| < 2.5$. We require one charged lepton pair of the same flavor and opposite sign, whose invariant mass well reconstructs the Z-boson, $|m_{\ell\ell} - m_Z| < 15$ GeV. For the hadronic part of the event, we demand at least four jets, where two are b-tagged. Jets are defined with the anti-k_T jet algorithm with radius $R = 0.5$ and $p_{Tj} > 30$ GeV using FASTJET [47]. As the signal displays a semileptonic top pair final state, it results in a considerable amount of missing energy stemming from the missing neutrino. Hence, it is required sizable transverse missing energy $\not{E}_T > 30$ GeV.

Since our signal can display a resonant behavior on the invariant mass m_{tt}, as well as m_{Ztt}, our analysis explores the profile of the two-dimensional distribution (m_{tt}, m_{Ztt}) to achieve a superior signal identification. Thus, we reconstruct the missing neutrino from the leptonic top decay. In our signal events, the measured $\not{E}_T$ comes mainly from the transverse momentum of the neutrino. Using the third lepton, we calculate the longitudinal component of the neutrino by using the W-boson mass constraint, which in most cases will provide two solutions for the neutrino momentum. The reconstruction of the top-quarks is performed by iterating over all possible partitions of light and b-tagged jets, forming the leptonic $(\ell\nu b)$ and hadronic (jjb) top-quarks. The two possible neutrino solutions are individually accounted for, which constitute different partitions. We chose the combination that minimizes

$$(m_{\ell\nu b} - m_t)^2 + (m_{jjb} - m_t)^2, \qquad (6)$$

where m_t is the on-shell top-quark mass. With the reconstructed top-quarks, we can examine the invariant masses m_{tt} and m_{Ztt}, which capture the resonant profile from H and A decays, arising from the loop-induced gluon fusion $gg \to A/H \to ZH/A$ and bottom quark-initiated $b\bar{b} \to A/H \to ZH/A$ contributions.

To estimate the high luminosity LHC sensitivity to Higgstrahlung signals $pp \to Z(\ell\ell)H(t\bar{t})$ and $pp \to Z(\ell\ell)A(t\bar{t})$, we performed a binned log-likelihood analysis based on the two-dimensional distribution (m_{tt}, m_{Ztt}). For illustration, the 2D distribution in $m_{tt} - m_{Ztt}$ plane for $m_A = 750$ GeV and $m_H = 600$ GeV is shown in Fig. 4 with $\Gamma_{A,H}/m_{A,H} = 1\%$ and $\Gamma_{A,H}/m_{A,H} = 10\%$. The correspondent $t\bar{t}Z$ background distribution is also shown. In Fig. 5, we present the resulting upper limit on the signal cross-section for $Z(\ell\ell)H(t\bar{t})$ and $Z(\ell\ell)A(t\bar{t})$ production at 95% confidence level (CL). The results are shown for several hypotheses of scalar and pseudoscalar widths.[4] We assume the HL-LHC with integrated luminosity $\mathcal{L} = 3\ \mathrm{ab}^{-1}$. The binned likelihood analysis is sensitive to the width dependence, leading to weaker results in the augmented $\Gamma_{H,A}/m_{H,A}$ regime. This is mostly a result of the enhanced negative contribution from the triangle-box interference for larger widths. The large interference effects and broader resonance from large width lead to suppressed signal events, which can be observed in Fig. 3 and Fig. 4. While we present the results in Fig. 5 following a model-independent approach similar to the CMS study in Ref. [46], in Sec. V C we perform a uniform parameter space scan considering the 2HDM in the type-I scenario.

---

[3] The dependence of the A and H widths with t_β and $c_{\beta-\alpha}$ is not included here. The effects from the change of the width have already been taken into account when we perform the simulation on the grid and interpolate the results.

[4] More results can be found at https://github.com/ycwu1030/AZH_Worker, where the analysis is saved.

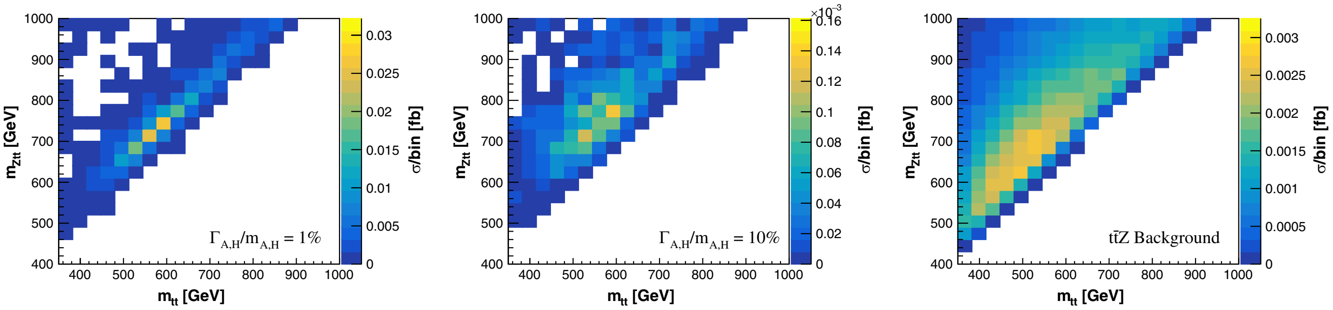

FIG. 4. The 2D distribution in $m_{tt} - m_{Ztt}$ plane for $m_A = 750$ GeV and $m_H = 600$ GeV with $\Gamma_{A,H}/m_{A,H} = 1\%$ (left panel) and $\Gamma_{A,H}/m_{A,H} = 10\%$ (middle panel). The $t\bar{t}Z$ background is also presented (right panel). The cross-section around the white pixels are either not kinematically allowed (right region) or suppressed (top left region), and we could not find any events in our scan.

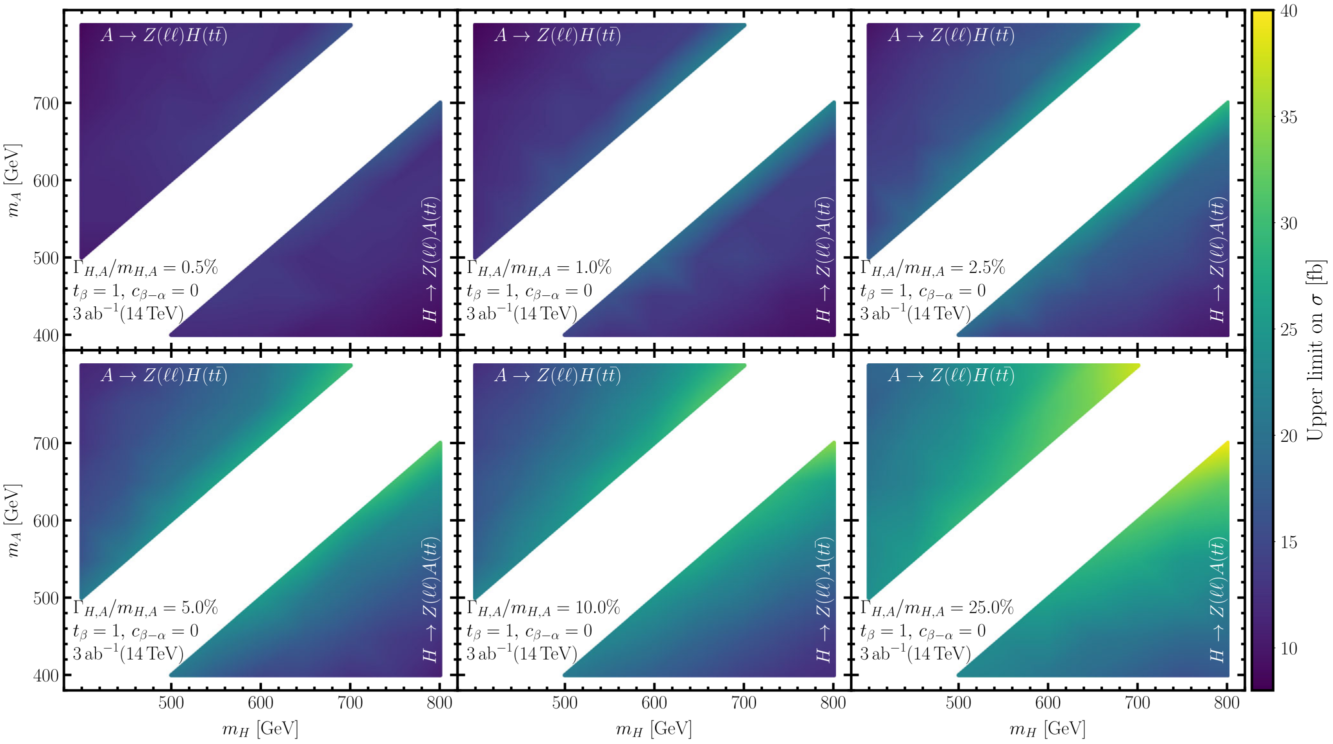

FIG. 5. 95% C.L. upper limit on the cross-section $\sigma(pp \to ZH/A) \times \text{BR}(H/A \to t\bar{t})$ in the $m_A - m_H$ plane, with different choice of widths for the H and A bosons. We consider the $\sqrt{s} = 14$ TeV HL-LHC with 3 ab^{-1} of integrated luminosity.

V. ELECTROWEAK PHASE TRANSITION IN THE 2HDM

In this section, we study the complementarity between collider and gravitational wave experiments to probe the phase transition profile in the 2HDM. We first define the one-loop effective potential at finite temperature in Sec. V A, then discuss important ingredients for calculating the EWPT and gravitational wave sensitivity at space-based experiments in Sec. V B. Finally, we analyze in Sec. V C the relevance of the Higgstrahlung channel with top pair final states $H/A \to t\bar{t}$ with respect to other relevant classes of searches at the HL-LHC and also contrast the collider with the gravitational wave sensitivity.

A. Finite temperature effective potential

In order to study the thermal history of the 2HDM, one needs to study the loop-corrected effective potential at finite temperature. It is defined by the addition of the tree-level potential V_0, the zero-temperature one-loop corrections from the Coleman-Weinberg potential V_{CW} with the respective counter terms V_{CT}, and the one-loop thermal corrections V_T. Thus, the final potential can be written as

$$V_{\text{eff}} = V_0 + V_{\text{CW}} + V_{\text{CT}} + V_T. \tag{7}$$

The zero-temperature one-loop correction in the $\overline{\text{MS}}$ have the form [48]

$$V_{\mathrm{CW}} = \sum_i \frac{n_i}{64\pi^2} m_i^4(\Phi_1,\Phi_2)\left[\log\left(\frac{m_i^2(\Phi_1,\Phi_2)}{\mu^2}\right) - c_i\right], \tag{8}$$

where $m_i(\Phi_1,\Phi_2)$ is the field-dependent mass of the particle of type i, with n_i being the correspondent number of degrees of freedom. We define $n_i > 0$ for bosons and $n_i < 0$ for fermions. The renormalization scale constant is set to the electroweak VEV at zero-temperature, $\mu = v \approx 246$ GeV. The c_i are the renormalization constants in the $\overline{\mathrm{MS}}$ scheme, with $c_i = 5/6$ for gauge bosons and $c_i = 3/2$ for scalars and fermions. The Coleman-Weinberg potential was evaluated in the Landau gauge, allowing for the omission of ghost contributions.

In principle, the tree-level scalar masses and mixing angles are shifted by the addition of the Coleman-Weinberg potential. To make our parameter space scan more efficient, we follow a renormalization prescription that requires these parameters to match their tree-level values [20,49]. We achieve this by adding the counterterms

$$\begin{aligned} V_{CT} = {} & \delta m_{11}^2 \Phi_1^\dagger\Phi_1 + \delta m_{22}^2 \Phi_2^\dagger\Phi_2 - \delta m_{12}^2(\Phi_1^\dagger\Phi_2 + \mathrm{H.c.}) \\ & + \frac{\delta\lambda_1}{2}(\Phi_1^\dagger\Phi_1)^2 + \frac{\delta\lambda_2}{2}(\Phi_2^\dagger\Phi_2)^2 \\ & + \delta\lambda_3(\Phi_1^\dagger\Phi_1)(\Phi_2^\dagger\Phi_2) + \delta\lambda_4(\Phi_1^\dagger\Phi_2)(\Phi_2^\dagger\Phi_1) \\ & + \frac{\delta\lambda_5}{2}((\Phi_1^\dagger\Phi_2)^2 + \mathrm{H.c.}), \end{aligned} \tag{9}$$

imposing the following renormalization conditions at zero-temperature

$$\partial_{\phi_i}(V_{\mathrm{CW}} + V_{\mathrm{CT}})|_{\omega=\omega_{\mathrm{tree}}} = 0, \tag{10}$$

$$\partial_{\phi_i}\partial_{\phi_j}(V_{\mathrm{CW}} + V_{\mathrm{CT}})|_{\omega=\omega_{\mathrm{tree}}} = 0, \tag{11}$$

where ω_{tree} generically stands for the minimum of the tree-level potential for the ϕ_i fields. Eq. (10) requires that the zero-temperature minimum matches the tree-level value. Similarly, Eq. (11) demands that $T = 0$ masses and mixing angles do not change with respect to the tree-level numbers.

The one-loop thermal corrections read [50]

$$\begin{aligned} V_T = {} & \frac{T^4}{2\pi^2}\left[\sum_f n_f J_+\left(\frac{m_f^2}{T^2}\right) + \sum_{\mathcal{V}_T} n_{\mathcal{V}_T} J_-\left(\frac{m_{\mathcal{V}_T}^2}{T^2}\right) \right. \\ & \left. + \sum_{\mathcal{V}_L} n_{\mathcal{V}_L} J_-\left(\frac{m_{\mathcal{V}_L}^2}{T^2}\right)\right] - \frac{T^4}{2\pi^2}\sum_{\mathcal{V}_L}\frac{\pi}{6}\left(\frac{\bar{m}_{\mathcal{V}_L}^3}{T^3} - \frac{m_{\mathcal{V}_L}^3}{T^3}\right), \end{aligned} \tag{12}$$

where f, $\mathcal{V}_T$, and $\mathcal{V}_L$ indicate respectively the sum over fermions, transverse gauge bosons (W_T, Z_T), and longitudinal modes of gauge bosons and scalars ($W_L, Z_L, \gamma_L, \Phi^0, \Phi^\pm$). The second line of Eq. (12) corresponds to the daisy contributions, following the Arnold-Espinosa scheme [20,50]. Finally, the thermal functions J_+ and J_- are given by

$$J_\pm(x) = \mp\int_0^\infty dy\, y^2 \log\left(1 \pm e^{-\sqrt{y^2+x^2}}\right). \tag{13}$$

B. Thermal history and gravitational waves

The rich structure of the 2HDM potential grants distinct phase transition processes. For successful baryogenesis, it is critical to prevent the baryon number generated during the phase transition from being significantly washed out. This imposes the electroweak phase transition to be strong first-order [51,52]

$$\xi_c \equiv \frac{v_c}{T_c} \gtrsim 1, \tag{14}$$

where T_c is the critical temperature and v_c is the critical Higgs VEV obtained when the would-be true vacuum and false vacuum are degenerate.

The occurrence of phase transition depends on the false to true vacuum tunneling rate, which is given by [53,54]

$$\Gamma(T) \approx T^4\left(\frac{S_3}{2\pi T}\right)^{3/2} e^{-\frac{S_3}{T}}, \tag{15}$$

where S_3 denotes the three-dimensional Euclidean action that can be expressed as

$$S_3 = 4\pi\int_0^\infty dr r^2\left[\frac{1}{2}\left(\frac{d\phi(r)}{dr}\right)^2 + V(\phi,T)\right]. \tag{16}$$

To obtain the nucleation rate, we need to calculate the scalar field ϕ bubble profile by solving the bounce equation

$$\frac{d^2\phi}{dr^2} + \frac{2}{r}\frac{d\phi}{dr} = \frac{dV(\phi,T)}{d\phi}, \tag{17}$$

with boundary conditions

$$\lim_{r\to\infty}\phi(r) = 0 \quad \text{and} \quad \lim_{r\to 0}\frac{d\phi(r)}{dr} = 0. \tag{18}$$

We solve the differential equation and calculate S_3 with CosmoTransitions v2.0.5 [55]. The nucleation onsets at temperature T_n, where one bubble nucleates per horizon volume. This condition can be approximated for EWPT as $S_3(T_n)/T_n \approx 140$ [56].

We can now define the quantities β and α that describe the dynamical properties of the phase transition, which can be used to model the strength of stochastic gravitational wave signals [7,57]. The inverse time duration of phase transition β/H_n is defined as

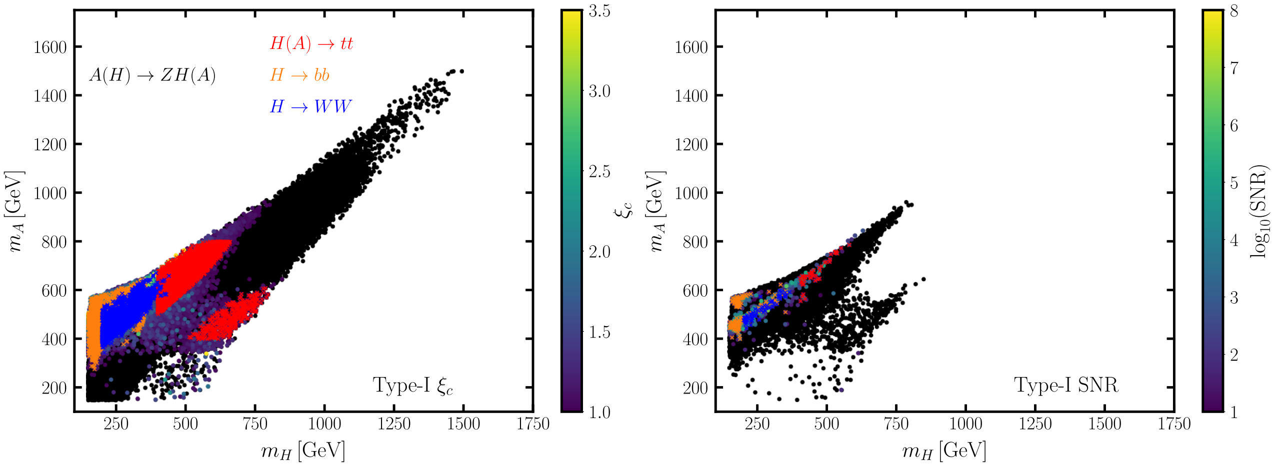

FIG. 6. The $pp \to ZH/A$ constraints on $m_H - m_A$ plane. The heat map tracks ξ_c (left panel) and SNR (right panel). For the left panel, the black points represent the parameter space regime with first-order phase transition with $\xi_c > 0$. For the right panel, the black points indicate the regime with $\xi_c > 1$. The parameter space scan is performed with Scanners [59], where the constraints from perturbative unitarity, boundness from below, vacuum stability, electroweak precision, and flavor constraints are imposed. HiggsBounds and HiggsSignals are also included to incorporate the searches for additional scalars as well as the 125 GeV Higgs boson measurement [66,67]. The colored crosses are points with $\xi_c > 1$ that can be probed by the HL-LHC through $pp \to ZH/A$ ($Z \to \ell\ell$) channel with $H/A \to t\bar{t}$ (red), $H \to b\bar{b}$ (orange), and $H \to WW$ (blue).

$$\frac{\beta}{H_n} \equiv T_n \frac{d}{dT}\left(\frac{S_3}{T}\right)\bigg|_{T=T_n}, \tag{19}$$

where H_n is the Hubble constant at T_n. The other important parameter α characterizes the ratio between the latent heat released during the phase transition (ϵ) with respect to the radiation energy density ($\rho_{\rm rad}$), $\alpha \equiv \epsilon/\rho_{\rm rad}$. These parameters are given by

$$\epsilon = \Delta\left(-V_{\rm eff} + T\frac{\partial V_{\rm eff}}{\partial T}\right)_{T=T_n} \quad \text{and} \quad \rho_{\rm rad} = \frac{\pi^2}{30} g_\star T_n^4, \tag{20}$$

with $g_\star$ being the number of relativistic degrees of freedom in the thermal plasma. Here, Δ denotes the difference between true and false vacua.

We are able to estimate the sensitivity of gravitational wave experiments, adopting the signal-to-noise ratio (SNR) measure [57]

$$\text{SNR} = \sqrt{\mathcal{T}\int_{f_{\rm min}}^{f_{\rm max}} df \left[\frac{h^2\Omega_{\rm GW}(f)}{h^2\Omega_{\rm Sens}(f)}\right]^2}, \tag{21}$$

where $\mathcal{T}$ is the duration of the mission and $\Omega_{\rm Sens}$ is the sensitivity profile of the particular GW experiment [8]. In our analysis, we consider the space-based LISA experiment, assuming $\mathcal{T} = 5$ years and SNR > 10 to characterize signal detection [57].

C. Probing EWPT in the 2HDM

In this section, we examine the sensitivity of the resonant top pair searches to the parameter space regime related to SFOEWPT in the 2HDM. Instead of performing a model-independent analysis as in Fig. 5, we implement a uniform parameter space scan of the 2HDM for the type-I scenario. The uniformly random scan is performed over the region

$$\begin{aligned} &\tan\beta \in (0.8, 25), \qquad m_{12}^2 \in (10^{-3}, 10^5)\ \text{GeV}^2,\\ &m_H \in (150, 1500)\ \text{GeV},\\ &\cos(\beta-\alpha) \in (-0.3, 0.3), \qquad m_A \in (150, 1500)\ \text{GeV},\\ &m_{H^\pm} \in (150, 1500)\ \text{GeV}. \end{aligned} \tag{22}$$

The theoretical and experimental limits to the model are implemented with Scanners v2.0.0 [58,59]. With this package, we require constraints from perturbative unitarity [60–62], boundness from below [63], vacuum stability [64,65], flavor constraints, and electroweak precision. HiggsBounds v5.3.2 and HiggsSignals v2.2.3 are used to account for the heavy Higgs searches and the 125 GeV Higgs boson measurements [66,67].

The current experimental Higgstrahlung studies $pp \to ZH/A$ only account for the scalar decays $H/A \to b\bar{b}$ and $H \to WW$, associated with $Z \to \ell\ell$ [35,36]. In Fig. 6, we present the projection for these analyses to the HL-LHC luminosity $\mathcal{L} = 3$ ab^{-1}. The projected upper bounds on the cross-section for corresponding processes are compared with the cross-section times the branching fraction of each parameter point obtained from Scanners [59]. Both the bottom and W-boson final states will provide relevant sensitivity to SFOEWPT. Interestingly, the sensitivity of these channels is mostly restricted to the $m_{H,A} < 350$ GeV regime. Above the top-quark pair threshold, the $H/A \to t\bar{t}$ final state is typically the dominant scalar decay, favoring

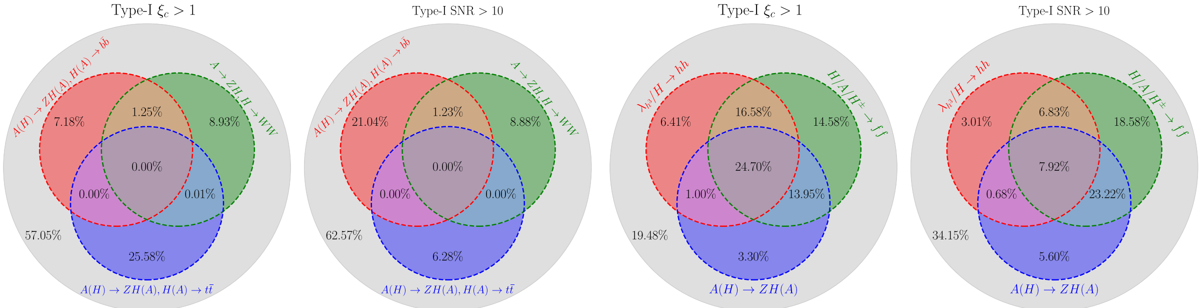

FIG. 7. Left: The summary of sensitivities for the Higgstrahlung search channels $pp \to ZH/A$ at the HL-LHC. The number in each region denotes the fraction of currently allowed points, by theoretical and experimental constraints, that will be probed by the Higgstrahlung $b\bar{b}$, WW, and $t\bar{t}$ final state searches at the HL-LHC. Right: The summary of the capabilities of corresponding search channels including nonresonant and resonant double Higgs searches $\lambda_{h^3}/H \to hh$, fermionic decay channels $H/A/H^{\pm} \to ff$, and $A(H) \to ZH(A)$.

phenomenological analyses with a resonant top-quark pair final state. We present in Fig. 6 (red points) the results of our $pp \to Z(\ell\ell)H(t\bar{t})$ and $pp \to Z(\ell\ell)A(t\bar{t})$ analyzes, as described in Sec. III. We observe that the Higgstrahlung searches with $t\bar{t}$ final state largely extend the sensitivity to SFOEWPT.

In the left two panels of Fig. 7, we present a detailed comparison among the $b\bar{b}$, WW, and $t\bar{t}$ final states for the $pp \to ZH/A$ channel. The number in each region indicates the fraction of points in our uniformly random scan that can be excluded by the corresponding searches. They are the fraction of points currently allowed, under theoretical and experimental constraints, that will be probed at the HL-LHC. The first panel focuses on the SFOEWPT regime with $\xi_c > 1$ and the second one represents the points that can display gravitational wave signals at LISA with signal-to-noise ratio $\mathrm{SNR} > 10$. We observe from these Venn diagrams that the Higgstrahlung channels with top pair final states $pp \to ZH(t\bar{t})$ and $ZA(t\bar{t})$ cover a large portion of the allowed parameter space. Therefore, the inclusion of this channel in forthcoming experimental analyses is strongly motivated.

In the right two panels of Fig. 7, we show the comparison of the Higgstrahlung sensitivity at the HL-LHC with other relevant channels in the context of EWPT, namely resonant and nonresonant double Higgs searches $H \to hh$ (or λ_{h^3}) and $gg \to H/A \to t\bar{t}$ (or $H^{\pm} \to tb$) searches. The results from these other studies were obtained from Ref. [10]. We added further details for the $gg \to H/A \to t\bar{t}$ searches in the Appendix. The HL-LHC will be able to cover ≈80% of the available $\xi_c > 1$ parameter space in the type-I 2HDM scenario. While the considered channels present relevant complementarities, the Higgstrahlung mode and gluon fusion scalar production with subsequent decay to top-quark pair (or charged Higgs production with fermionic decay $H^{\pm} \to tb$) result in leading sensitivities.

VI. SUMMARY

The thermal history of electroweak symmetry breaking in the Universe could have profound consequences for particle physics and cosmology. In this article, we study the prospects for the HL-LHC to probe the strong first-order electroweak phase transition regime in the type-I 2HDM. We devote special attention to the Higgstrahlung channel $pp \to ZH/A$ with a resonant top-quark pair final state $H/A \to t\bar{t}$.

We scrutinize the signal components associated with this channel and find that it is important to go beyond the resonant $gg \to A/H \to ZH/A$ theoretical modeling, including the full signal simulation. The 2HDM can display large interference effects between the resonant and nonresonant $gg \to ZH/A$ production and augmented b-quark initiated contributions. Accounting for the theoretical and experimental constraints, we find that the considered Higgstrahlung final state $H/A \to t\bar{t}$ renders the largest sensitivity to the $\xi_c > 1$ regime in the 2HDM, in comparison to the other Higgstrahlung searches already accounted for by ATLAS and CMS, which rely on the $H/A \to b\bar{b}$ and $H \to WW$ final states.

Finally, we derive the complementarity of the Higgstrahlung searches with other relevant classes of searches at the HL-LHC (namely, resonant and nonresonant double Higgs searches and heavy scalar decays to fermions $A/H/H^{\pm} \to ff$) and confront with the gravitational wave sensitivity at LISA. We obtain that the channel studied here, with top-quark pair final state, will be a promising signature for $\xi_c > 1$ at the HL-LHC. Therefore, the inclusion of the studied Higsstrahlung channel in the forthcoming ATLAS and CMS experimental analyses is strongly motivated, as it would both augment the sensitivity to the 2HDM parameter space and substantially boost the sensitivity to SFOEWPT at the LHC.

ACKNOWLEDGMENTS

D. G., A. K., and Y. W. thank the U.S. Department of Energy for financial support, under Grant No. DE-SC 0016013. Some computing for this project was performed at the High-Performance Computing Center at Oklahoma State University, supported in part through the National Science Foundation Grant No. OAC-1531128.

APPENDIX: TOP PAIR RESONANT SEARCHES VIA $gg \to H/A \to t\bar{t}$

In this appendix, we briefly review the top-quark pair resonant searches via gluon fusion $gg \to H/A \to t\bar{t}$. The gluon fusion channel displays sizable interference effects between the s-channel (pseudo)scalar induced top pair production (left diagram of Fig. 8) and the QCD top pair production (middle and right diagrams of Fig. 8) [68–84]. The large interference has significant phenomenological consequences, since the top-quark invariant mass m_{tt} does not display a simple resonance profile around the (pseudo) scalar mass $m_{H/A}$, instead it presents a bump-dip shape.

In Fig. 9, we show the top pair invariant mass distribution m_{tt} at the parton level for the CP-even scalar H (left panel) and CP-odd mode A (right panel). The signal-only resonant profiles are shown by the dashed curves, while the full signal contributions, which account for interference effects, are shown in the solid curves. Interferences highly depend on the scalar width. Hence, in Fig. 9, the distributions are shown for two different choices of width: $\Gamma_{H/A}/m_{H/A} = 5\%$ (blue) and $\Gamma_{H/A}/m_{H/A} = 10\%$ (red). It is clear that the resonant shape from the signal-only sample changes into a bump-dip shape when accounting for the interference with the QCD top-quark pair production. Thus, it is necessary to include these effects to generate robust phenomenological modeling for the signal sample.

Current ATLAS and CMS analyses for resonant top-quark pair production account for the interferences with the SM $t\bar{t}$ production [46,85]. In particular, the more recent CMS results are presented as upper limits on the coupling of the scalar to the top-quark pair as a function of the scalar mass and width. When we apply such constraints for each parameter point, the total width of the corresponding scalar is calculated. Then, the upper bound on the coupling of the scalar to top-quark pair is obtained by interpolating the results from the experimental results for the corresponding scalar mass. This upper bound is then compared with the actual coupling for this parameter point. This analysis can be translated into constraints on the 2HDM parameter space. Remarkably, it is found that the top-quark pair searches $gg \to H/A \to t\bar{t}$ can cover a large portion of the parameter space sensitive SFOEWPT in the 2HDM [10].

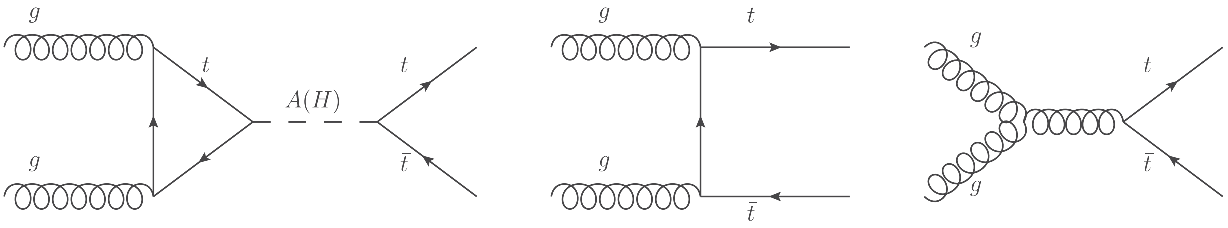

FIG. 8. Representative set of Feynman diagrams for the top-quark pair production through scalar resonance $gg \to A/H \to t\bar{t}$ (left) and directly from gluon fusion $gg \to t\bar{t}$ (middle and right).

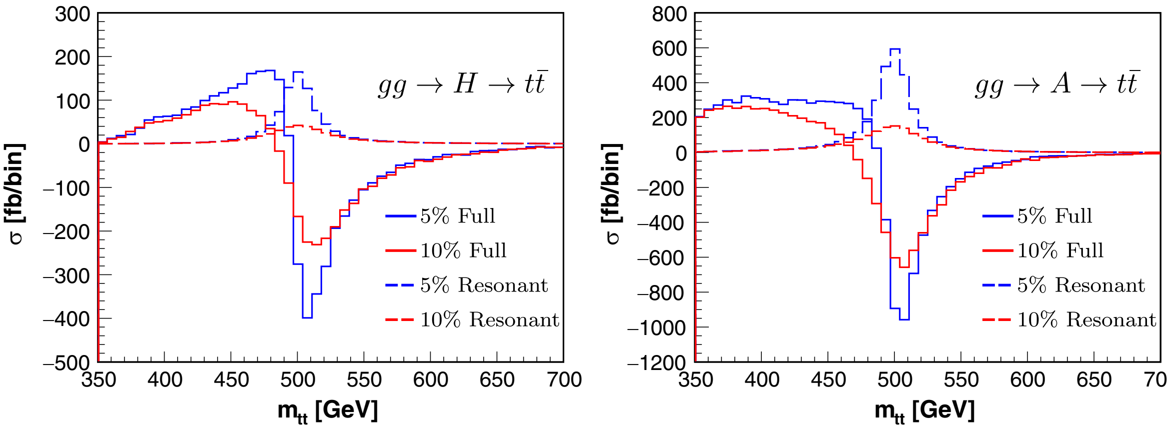

FIG. 9. The parton level distributions of m_{tt} from resonant production only (dashed curves) and with interference effects (solid curves) with two choices of the scalar width: $\Gamma_{H/A}/m_{H/A} = 5\%$ (blue) and $\Gamma_{H/A}/m_{H/A} = 10\%$ (red), assuming $m_{H/A} = 500$ GeV, $t_\beta = 1$ and $c_{\beta-\alpha} = 0$.

[1] K. Kajantie, M. Laine, K. Rummukainen, and M. E. Shaposhnikov, Is there a Hot Electroweak Phase Transition at m(H) Larger or Equal to m(W)?, Phys. Rev. Lett. **77**, 2887 (1996).

[2] A. D. Sakharov, Violation of *CP* Invariance, C asymmetry, and baryon asymmetry of the universe, Pis'ma Zh. Eksp. Teor. Fiz. **5**, 32 (1967).

[3] M. Trodden, Electroweak baryogenesis, Rev. Mod. Phys. **71**, 1463 (1999).

[4] A. G. Cohen, D. B. Kaplan, and A. E. Nelson, Progress in electroweak baryogenesis, Annu. Rev. Nucl. Part. Sci. **43**, 27 (1993).

[5] M. Carena, M. Quiros, and C. E. M. Wagner, Opening the window for electroweak baryogenesis, Phys. Lett. B **380**, 81 (1996).

[6] D. E. Morrissey and M. J. Ramsey-Musolf, Electroweak baryogenesis, New J. Phys. **14**, 125003 (2012).

[7] C. Grojean and G. Servant, Gravitational waves from phase transitions at the electroweak scale and beyond, Phys. Rev. D **75**, 043507 (2007).

[8] H. Audley *et al.* (LISA Collaboration), Laser interferometer space antenna, arXiv:1702.00786.

[9] M. J. Ramsey-Musolf, The electroweak phase transition: A collider target, J. High Energy Phys. 09 (2020) 179.

[10] D. Gonçalves, A. Kaladharan, and Y. Wu, Electroweak phase transition in the 2HDM: Collider and gravitational wave complementarity, Phys. Rev. D **105**, 095041 (2022).

[11] O. J. P. Eboli, G. C. Marques, S. F. Novaes, and A. A. Natale, Twin Higgs boson production, Phys. Lett. B **197**, 269 (1987).

[12] T. Plehn, M. Spira, and P. M. Zerwas, Pair production of neutral Higgs particles in gluon-gluon collisions, Nucl. Phys. **B479**, 46 (1996).

[13] J. M. No and M. Ramsey-Musolf, Probing the Higgs portal at the LHC through resonant di-Higgs production, Phys. Rev. D **89**, 095031 (2014).

[14] D. Gonçalves, T. Han, F. Kling, T. Plehn, and M. Takeuchi, Higgs boson pair production at future hadron colliders: From kinematics to dynamics, Phys. Rev. D **97**, 113004 (2018).

[15] R. K. Barman, C. Englert, D. Gonçalves, and M. Spannowsky, Di-Higgs resonance searches in weak boson fusion, Phys. Rev. D **102**, 055014 (2020).

[16] G. Dorsch, S. Huber, K. Mimasu, and J. No, The Higgs vacuum uplifted: Revisiting the electroweak phase transition with a second Higgs doublet, J. High Energy Phys. 12 (2017) 086.

[17] H. Weicong, K. Zhaofeng, S. Jing, W. Peiwen, and Y. Jin, Min, New insights in the electroweak phase transition in the NMSSM, Phys. Rev. D **91**, 025006 (2015).

[18] C. Harman and S. Huber, Does zero temperature decide on the nature of the electroweak phase transition?, J. High Energy Phys. 06 (2016) 005.

[19] G. C. Dorsch, S. J. Huber, and J. M. No, A strong electroweak phase transition in the 2HDM after LHC8, J. High Energy Phys. 10 (2013) 029.

[20] P. Basler, M. Krause, M. Muhlleitner, J. Wittbrodt, and A. Wlotzka, Strong first order electroweak phase transition in the *CP*-conserving 2HDM revisited, J. High Energy Phys. 02 (2017) 121.

[21] G. C. Dorsch, S. J. Huber, K. Mimasu, and J. M. No, Hierarchical versus degenerate 2HDM: The LHC run 1 legacy at the onset of run 2, Phys. Rev. D **93**, 115033 (2016).

[22] J. Bernon, L. Bian, and Y. Jiang, A new insight into the phase transition in the early Universe with two Higgs doublets, J. High Energy Phys. 05 (2018) 151.

[23] J. O. Andersen, T. Gorda, A. Helset, L. Niemi, T. V. I. Tenkanen, A. Tranberg, A. Vuorinen, and D. J. Weir, Nonperturbative Analysis of the Electroweak Phase Transition in the Two Higgs Doublet Model, Phys. Rev. Lett. **121**, 191802 (2018).

[24] K. Kainulainen, V. Keus, L. Niemi, K. Rummukainen, T. V. I. Tenkanen, and V. Vaskonen, On the validity of perturbative studies of the electroweak phase transition in the Two Higgs Doublet model, J. High Energy Phys. 06 (2019) 075.

[25] W. Su, A. G. Williams, and M. Zhang, Strong first order electroweak phase transition in 2HDM confronting future Z & Higgs factories, J. High Energy Phys. 04 (2021) 219.

[26] S. Li, H. Song, and S. Su, Probing exotic charged Higgs decays in the type-II 2HDM through top rich signal at a future 100 TeV pp collider, J. High Energy Phys. 11 (2020) 105.

[27] F. Kling, S. Su, and W. Su, 2HDM neutral scalars under the LHC, J. High Energy Phys. 06 (2020) 163.

[28] H. Davoudiasl, I. M. Lewis, and M. Sullivan, Multi-TeV signals of baryogenesis in a Higgs troika model, Phys. Rev. D **104**, 015024 (2021).

[29] T. Biekötter, S. Heinemeyer, J. M. No, M. O. Olea, and G. Weiglein, Fate of electroweak symmetry in the early Universe: Non-restoration and trapped vacua in the N2HDM, J. Cosmol. Astropart. Phys. 06 (2021) 018.

[30] M. Aoki, T. Komatsu, and H. Shibuya, Possibility of multi-step electroweak phase transition in the two Higgs doublet models, Prog. Theor. Exp. Phys. **2022**, 063B05 (2022).

[31] K. Enomoto, S. Kanemura, and Y. Mura, Electroweak baryogenesis in aligned two Higgs doublet models, J. High Energy Phys. 01 (2022) 104.

[32] O. Atkinson, M. Black, C. Englert, A. Lenz, A. Rusov, and J. Wynne, The flavourful present and future of 2HDMs at the collider energy frontier, J. High Energy Phys. 11 (2022) 139.

[33] Anisha, L. Biermann, C. Englert, and M. Mühlleitner, Two Higgs doublets, Effective Interactions and a Strong First-Order Electroweak Phase Transition, J. High Energy Phys. 08 (2022) 091.

[34] G. C. Dorsch, S. J. Huber, K. Mimasu, and J. M. No, Echoes of the Electroweak Phase Transition: Discovering a second Higgs doublet through $A_0 \to ZH_0$, Phys. Rev. Lett. **113**, 211802 (2014).

[35] G. Aad *et al.* (ATLAS Collaboration), Search for a heavy Higgs boson decaying into a Z boson and another heavy Higgs boson in the $\ell\ell bb$ and $\ell\ell WW$ final states in pp collisions at $\sqrt{s} = 13$ TeV with the ATLAS detector, Eur. Phys. J. C **81**, 396 (2021).

[36] A. M. Sirunyan *et al.* (CMS Collaboration), Search for new neutral Higgs bosons through the $\mathrm{H} \to \mathrm{ZA} \to \ell^+\ell^-\mathrm{b}\bar{\mathrm{b}}$ process in pp collisions at $\sqrt{s} = 13$ TeV, J. High Energy Phys. 03 (2020) 055.

[37] G. C. Branco, P. M. Ferreira, L. Lavoura, M. N. Rebelo, M. Sher, and J. P. Silva, Theory and phenomenology of two-Higgs-doublet models, Phys. Rep. **516**, 1 (2012).
[38] J. F. Gunion and H. E. Haber, The *CP* conserving two Higgs doublet model: The approach to the decoupling limit, Phys. Rev. D **67**, 075019 (2003).
[39] T. Han, S. Li, S. Su, W. Su, and Y. Wu, Comparative studies of 2HDMs under the Higgs boson precision measurements, J. High Energy Phys. 01 (2021) 045.
[40] D. Goncalves, F. Krauss, S. Kuttimalai, and P. Maierhöfer, Higgs-strahlung: Merging the NLO Drell-Yan and loop-induced $0+1$ jet multiplicities, Phys. Rev. D **92**, 073006 (2015).
[41] J. Alwall, R. Frederix, S. Frixione, V. Hirschi, F. Maltoni, O. Mattelaer, H.-S. Shao, T. Stelzer, P. Torrielli, and M. Zaro, The automated computation of tree-level and next-to-leading order differential cross sections, and their matching to parton shower simulations, J. High Energy Phys. 07 (2014) 079.
[42] A. Alloul, N. D. Christensen, C. Degrande, C. Duhr, and B. Fuks, FeynRules 2.0—A complete toolbox for tree-level phenomenology, Comput. Phys. Commun. **185**, 2250 (2014).
[43] C. Degrande, Automatic evaluation of UV and R2 terms for beyond the standard model lagrangians: A proof-of-principle, Comput. Phys. Commun. **197**, 239 (2015).
[44] T. Sjöstrand, S. Ask, J. R. Christiansen, R. Corke, N. Desai, P. Ilten, S. Mrenna, S. Prestel, C. O. Rasmussen, and P. Z. Skands, An introduction to PYTHIA 8.2, Comput. Phys. Commun. **191**, 159 (2015).
[45] J. de Favereau, C. Delaere, P. Demin, A. Giammanco, V. Lemaître, A. Mertens, and M. Selvaggi (DELPHES 3 Collaboration), DELPHES 3, A modular framework for fast simulation of a generic collider experiment, J. High Energy Phys. 02 (2014) 057.
[46] A. M. Sirunyan *et al.* (CMS Collaboration), Search for heavy Higgs bosons decaying to a top quark pair in proton-proton collisions at $\sqrt{s} = 13$ TeV, J. High Energy Phys. 04 (2020) 171.
[47] M. Cacciari, G. P. Salam, and G. Soyez, FastJet user manual, Eur. Phys. J. C **72**, 1896 (2012).
[48] S. Coleman and E. Weinberg, Radiative corrections as the origin of spontaneous symmetry breaking, Phys. Rev. D **7**, 1888 (1973).
[49] J. E. Camargo-Molina, A. P. Morais, R. Pasechnik, M. O. P. Sampaio, and J. Wessén, All one-loop scalar vertices in the effective potential approach, J. High Energy Phys. 08 (2016) 073.
[50] P. B. Arnold and O. Espinosa, The effective potential and first order phase transitions: Beyond leading-order, Phys. Rev. D **47**, 3546 (1993).
[51] G. D. Moore, Measuring the broken phase sphaleron rate nonperturbatively, Phys. Rev. D **59**, 014503 (1999).
[52] M. Quiros, Finite temperature field theory and phase transitions, in *ICTP Summer School in High-Energy Physics and Cosmology* (World Scientific, Singapore, 1999), arXiv:hep-ph/9901312.
[53] A. D. Linde, Fate of the false vacuum at finite temperature: Theory and applications, Phys. Lett. B **100**, 37 (1981).
[54] S. R. Coleman, The fate of the false vacuum. 1. Semiclassical theory, Phys. Rev. D **15**, 2929 (1977).
[55] C. L. Wainwright, CosmoTransitions: Computing cosmological phase transition temperatures and bubble profiles with multiple fields, Comput. Phys. Commun. **183**, 2006 (2012).
[56] J. M. Moreno, M. Quiros, and M. Seco, Bubbles in the supersymmetric standard model, Nucl. Phys. **B526**, 489 (1998).
[57] C. Caprini *et al.*, Science with the space-based interferometer eLISA. II: Gravitational waves from cosmological phase transitions, J. Cosmol. Astropart. Phys. 04 (2016) 001.
[58] R. Coimbra, M. O. P. Sampaio, and R. Santos, ScannerS: Constraining the phase diagram of a complex scalar singlet at the LHC, Eur. Phys. J. C **73**, 2428 (2013).
[59] M. Mühlleitner, M. O. P. Sampaio, R. Santos, and J. Wittbrodt, ScannerS: Parameter scans in extended scalar sectors, Eur. Phys. J. C **82**, 198 (2022).
[60] B. W. Lee, C. Quigg, and H. B. Thacker, Weak interactions at very high-energies: The role of the Higgs boson mass, Phys. Rev. D **16**, 1519 (1977).
[61] S. Kanemura, T. Kubota, and E. Takasugi, Lee-Quigg-Thacker bounds for Higgs boson masses in a two doublet model, Phys. Lett. B **313**, 155 (1993).
[62] I. F. Ginzburg and I. P. Ivanov, Tree-level unitarity constraints in the most general 2HDM, Phys. Rev. D **72**, 115010 (2005).
[63] I. P. Ivanov, M. Köpke, and M. Mühlleitner, Algorithmic boundedness-from-below conditions for generic scalar potentials, Eur. Phys. J. C **78**, 413 (2018).
[64] W. G. Hollik, G. Weiglein, and J. Wittbrodt, Impact of vacuum stability constraints on the phenomenology of supersymmetric models, J. High Energy Phys. 03 (2019) 109.
[65] P. M. Ferreira, M. Mühlleitner, R. Santos, G. Weiglein, and J. Wittbrodt, Vacuum instabilities in the N2HDM, J. High Energy Phys. 09 (2019) 006.
[66] P. Bechtle, D. Dercks, S. Heinemeyer, T. Klingl, T. Stefaniak, G. Weiglein, and J. Wittbrodt, HiggsBounds-5: Testing Higgs sectors in the LHC 13 TeV era, Eur. Phys. J. C **80**, 1211 (2020).
[67] P. Bechtle, S. Heinemeyer, T. Klingl, T. Stefaniak, G. Weiglein, and J. Wittbrodt, HiggsSignals-2: Probing new physics with precision Higgs measurements in the LHC 13 TeV era, Eur. Phys. J. C **81**, 145 (2021).
[68] K. J. F. Gaemers and F. Hoogeveen, Higgs production and decay into heavy flavors with the gluon fusion mechanism, Phys. Lett. **146B**, 347 (1984).
[69] D. Dicus, A. Stange, and S. Willenbrock, Higgs decay to top quarks at hadron colliders, Phys. Lett. B **333**, 126 (1994).
[70] W. Bernreuther, M. Flesch, and P. Haberl, Signatures of Higgs bosons in the top quark decay channel at hadron colliders, Phys. Rev. D **58**, 114031 (1998).
[71] V. Barger, T. Han, and D. G. E. Walker, Top Quark Pairs at High Invariant Mass: A Model-Independent Discriminator of New Physics at the LHC, Phys. Rev. Lett. **100**, 031801 (2008).

[72] R. Frederix and F. Maltoni, Top pair invariant mass distribution: A window on new physics, J. High Energy Phys. 01 (2009) 047.

[73] R. Barcelo and M. Masip, Extra Higgs bosons in $t\bar{t}$ production at the LHC, Phys. Rev. D **81**, 075019 (2010).

[74] T. Figy and R. Zwicky, The other Higgses, at resonance, in the Lee-Wick extension of the Standard Model, J. High Energy Phys. 10 (2011) 145.

[75] V. Barger, W.-Y. Keung, and B. Yencho, Azimuthal correlations in top pair decays and the effects of new heavy scalars, Phys. Rev. D **85**, 034016 (2012).

[76] S. Moretti and D. A. Ross, On the top-antitop invariant mass spectrum at the LHC from a Higgs boson signal perspective, Phys. Lett. B **712**, 245 (2012).

[77] N. Craig, F. D'Eramo, P. Draper, S. Thomas, and H. Zhang, The hunt for the rest of the Higgs bosons, J. High Energy Phys. 06 (2015) 137.

[78] W. Bernreuther, P. Galler, C. Mellein, Z. G. Si, and P. Uwer, Production of heavy Higgs bosons and decay into top quarks at the LHC, Phys. Rev. D **93**, 034032 (2016).

[79] S. Gori, I.-W. Kim, N. R. Shah, and K. M. Zurek, Closing the wedge: Search strategies for extended Higgs sectors with heavy flavor final states, Phys. Rev. D **93**, 075038 (2016).

[80] A. Djouadi, J. Ellis, and J. Quevillon, Interference effects in the decays of spin-zero resonances into $\gamma\gamma$ and $t\bar{t}$, J. High Energy Phys. 07 (2016) 105.

[81] B. Hespel, F. Maltoni, and E. Vryonidou, Signal background interference effects in heavy scalar production and decay to a top-anti-top pair, J. High Energy Phys. 10 (2016) 016.

[82] M. Czakon, D. Heymes, and A. Mitov, Bump hunting in LHC $t\bar{t}$ events, Phys. Rev. D **94**, 114033 (2016).

[83] M. Carena and Z. Liu, Challenges and opportunities for heavy scalar searches in the $t\bar{t}$ channel at the LHC, J. High Energy Phys. 11 (2016) 159.

[84] A. Djouadi, J. Ellis, A. Popov, and J. Quevillon, Interference effects in $t\bar{t}$ production at the LHC as a window on new physics, J. High Energy Phys. 03 (2019) 119.

[85] M. Aaboud *et al.* (ATLAS Collaboration), Search for Heavy Higgs Bosons A/H Decaying to a Top Quark Pair in pp Collisions at $\sqrt{s} = 8$ TeV with the ATLAS Detector, Phys. Rev. Lett. **119**, 191803 (2017).